First-principles determination of the rhombohedral magnetostriction of $Fe_{100-x}Al_x$ and $Fe_{100-x}Ga_x$ alloys

Yanning Zhang,[1] Hui Wang,[1,2] and Ruqian Wu[1]

[1]*Department of Physics and Astronomy, University of California, Irvine, California, 92697-4575, USA*

[2]*Shenyang National Laboratory of Materials Science, Institute of Metal Research and International Centre of Materials Physics, Chinese Academy of Sciences, Shenyang, 110016, China*

(Received 20 August 2012; revised manuscript received 27 November 2012; published 14 December 2012)

Through systematic density functional calculations using the full potential linearized augmented plane-wave (FLAPW) method, the rhombohedral magnetostriction (λ_{111}) of $Fe_{100-x}Al_x$ and $Fe_{100-x}Ga_x$ alloys are studied for x up to 25. Theoretical calculations satisfactorily reproduce the main features of experimental $\lambda_{111}(x)$ curves, except for dilute alloys with $x < 5$. Detailed analyses on electronic and structural properties indicate the importance of availability and symmetry of dangling bonds for the sign change of λ_{111} around $x = 16$. In addition, the impurity induced local distortion might be a possible reason for the disagreement between theory and experiment for λ_{111} of the bulk bcc Fe.

DOI: 10.1103/PhysRevB.86.224410 PACS number(s): 75.80.+q, 71.15.Mb, 71.20.Be, 75.30.Gw

I. INTRODUCTION

Magnetostriction in a ferromagnetic material is the change of shape or dimension in response to the reorientation of magnetization along the applied external magnetic field.[1] Highly magnetostrictive rare-earth-free alloys such as $Fe_{100-x}Ga_x$ (Galfenol) and $Fe_{100-x}Al_x$ (Alfenol) have recently attracted extensive attention due to their excellent features including large strains at moderate fields, high permeability, and good ductility.[2–7] Tremendous efforts have been dedicated in the last decade to improve the performance of $Fe_{100-x}Ga_x$ and $Fe_{100-x}Al_x$ alloys[8,9] for applications in sensors, actuators, transducers, MEMS, and energy converting devices. The tetragonal magnetostrictive coefficient (λ_{100}) of $Fe_{100-x}Ga_x$ has an unique dependence on the composition of Ga, with two maxima at $x = 19$ and $x = 28$ in the $\lambda_{100}(x)$ curve, both above 300 ppm.[9] On the contrary, the rhombohedral magnetostrictive coefficient (λ_{111}) shows no measurable change for $x < 15$, but suddenly changes its sign near $x \approx 16$ from negative to positive. The origin of the diverging behaviors of tetragonal and rhombohedral magnetostrictive responses has not been well understood even after extensive interdisciplinary efforts.[6,8,9] Recent density functional theory (DFT) studies satisfactorily reproduced the experimental $\lambda_{100}(x)$ ($x < 19$) curves of $Fe_{100-x}Ga_x$.[10,11] As was also revealed in experiments,[12,13] the enhanced tetragonal magnetostriction of $Fe_{100-x}Ga_x$ and related alloys should be attributed to electronic factors rather than to motions of precipitates.[14] Nevertheless, calculations for λ_{111} of these alloys have never been done, and cross examinations for λ_{100} and λ_{111} are necessary to establish reliable theoretical models and insights.

Magnetostriction originates from spin-orbit coupling (SOC), which is typically rather weak in $3d$ transition metals.[15] DFT calculations of rhombohedral magnetostriction are still nontrivial even for very simple systems. In previous theoretical studies, Fähnle *et al.* obtained positive λ_{111} for the bulk bcc Fe using three different approaches, opposite in sign from experimental data: $\lambda_{111} = -21$ ppm.[16] The deficiency of the exchange-correlation potential was blamed for the description of Fe, but the actual reason for this "failure" remains mysterious. λ_{111} was found to be more sensitive than λ_{100} to the change of lattice size, the presence of impurities, or the slight change of s-d charge transfer. Studies of λ_{111} for complex alloys may provide more stringent tests for the reliability of DFT approaches for the determination of SOC-induced magnetic properties.

In this paper we report results of DFT calculations for λ_{111} of $Fe_{100-x}Al_x$ and $Fe_{100-x}Ga_x$ alloys with $x < 25$. The calculated values of λ_{111} are overall in good agreement with experiments, except for bcc Fe and dilute alloys with $x < 5$. The rhombohedral shear modulus (c_{44}) is almost independent of x and hence the magnetoelastic constant (b_2) determines the $\lambda_{111}(x)$ behavior. Extensive analysis reveals the key factors for the sign change of λ_{111} around $x = 16$ for $Fe_{100-x}Ga_x$ and $Fe_{100-x}Al_x$ alloys. Possible reasons that lead to different signs of λ_{111} between theory and experiment for the bulk Fe are also discussed.

II. COMPUTATIONAL DETAILS

For a cubic material, the field-induced fractional change in length $\Delta l/l_0$ can be expressed in terms of λ_{100} and λ_{111} as[1]

$$\frac{\Delta l}{l_0} = \frac{3}{2}\lambda_{100}\left(\sum_{i=1}^{3}\alpha_i^2\beta_i^2 - \frac{1}{3}\right) + 3\lambda_{111}(\alpha_1\alpha_2\beta_1\beta_2 + \alpha_2\alpha_3\beta_2\beta_3 + \alpha_3\alpha_1\beta_3\beta_1), \quad (1)$$

where l_0 is the length of an unmagnetized reference state, and α_i and β_i are directional cosines of the magnetization and the strain measurement with respect to the ith crystalline axis. The magnetostriction coefficient λ_{111} thus can be obtained by measuring $\Delta l/l_0$ along the (111) direction ($\beta_i = 1/\sqrt{3}$) when the magnetization direction is switched from the (111) axis to the $(11\bar{2})$ axis:

$$\lambda_{111} = -\frac{2}{3}\left(\left.\frac{\Delta l}{l_0}\right|_{11\bar{2}} - \left.\frac{\Delta l}{l_0}\right|_{111}\right) = -\frac{2}{3}\frac{l_0\left(\alpha_1 = \alpha_2 = \frac{1}{\sqrt{6}}, \alpha_3 = -\frac{2}{\sqrt{6}}\right) - l_0\left(\alpha_1 = \alpha_2 = \alpha_3 = \frac{1}{\sqrt{3}}\right)}{l_0\left(\alpha_1 = \alpha_2 = \alpha_3 = \frac{1}{\sqrt{3}}\right)}. \quad (2)$$

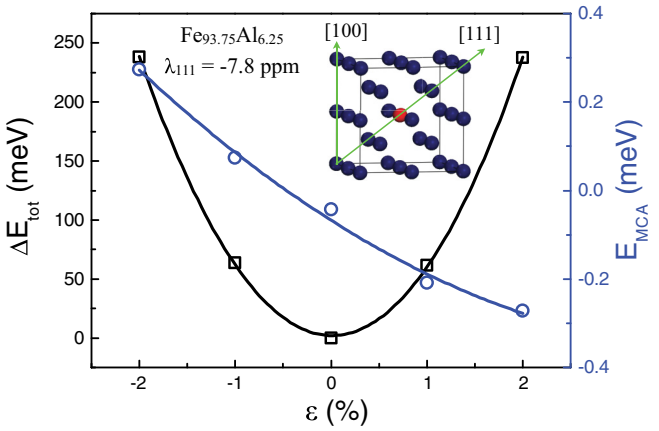

FIG. 1. (Color online) Calculated strain dependencies of $E_{\rm tot}$ (black open squares) and $E_{\rm MCA}$ (blue/gray open circles) of $Fe_{93.75}Al_{6.25}$. The inset is the atomic model used in the present calculations. Blue (dark gray) and red (light gray) balls represent the Fe and Al atoms, respectively.

In the present DFT calculations we applied rhombohedral strains [$\varepsilon = (l - l_0)/l_0$] along the (111) direction of the cubic unit cell in the constant-volume mode (i.e., $\varepsilon_{11\bar{2}} = -\varepsilon_{111}/2 = -\varepsilon/2$) and calculated the strain dependencies of magnetocrystalline anisotropy ($E_{\rm MCA} = E_{111} - E_{11\bar{2}}$) and total energy ($E_{\rm tot}$). The rhombohedral magnetostrictive coefficient λ_{111} can be directly calculated through the following equation:[16]

$$\lambda_{111} = \frac{2d E_{\rm MCA}/d\varepsilon}{3d^2 E_{\rm tot}/d\varepsilon^2} = -\frac{b_2}{3c_{44}}. \quad (3)$$

Here b_2 ($= -\frac{2}{3V}\frac{dE_{\rm MCA}}{d\varepsilon}$ in the present deformation mode, and V is the volume of the unit cell) and c_{44} ($= \frac{1}{3V}\frac{d^2E_{\rm tot}}{d\varepsilon^2}$) are the magnetoelastic and elastic stiffness constants, respectively.

We employed the highly precise full potential linearized augmented plane-wave (FLAPW) method that has no shape approximation for charge, potential, and wave function expansions.[17] The spin-polarized generalized gradient approximation (GGA) was used for the description of the exchange-correlation interaction among electrons.[18] The core electrons were treated fully relativistically, while the spin-orbit coupling term was invoked second variationally for the valence states. Energy cutoffs of 225 and 16 Ry were chosen for the plane-wave expansions of charge potential and basis in the interstitial region, respectively. In the muffin-tin region ($r_{\rm Fe} = 1.20$ Å, $r_{\rm Al} = 1.06$ Å, and $r_{\rm Ga} = 1.22$ Å), charge, potential, and basis functions were expanded in terms of spherical harmonics with a maximum angular momentum of $l_{\rm max} = 8$. Electronic self-consistence was assumed when the root-mean-square differences between the input and output charge and spin densities are less than 1.0×10^{-4} e/(a.u.).[3] The values of $E_{\rm MCA}$ were calculated through the torque approach.[15] Numerical convergence of all physical properties, particularly $E_{\rm MCA}$, against the number of k points in the Brillouin zone (BZ) was carefully monitored.

For the comparability we used identical 16-atom supercells as for the determination of tetragonal magnetostriction of $Fe_{100-x}Ga_x$ alloys at $x = 6.25$, 12.5, and 18.75 in our previous work.[10] In these configurations, different numbers of Al or Ga atoms were placed in the bcc lattices without Al or Ga first neighborhood, and the cubic symmetry of supercells was reserved (cf. the insets of Fig. 2 in Ref. 10 for details). For cases of $x = 1.85$ and 8.33 we placed metalloid atoms in larger supercells with either 54 or 24 atoms. For alloys with high Al/Ga concentrations, both B2 and $D0_3$ structures were examined, and the more stable $D0_3$ structure was used for studies of physical properties of $Fe_{75}Al_{25}$. Nevertheless, $D0_3$ structure was found to be unstable for $Fe_{75}Ga_{25}$ and we thereby limited our studies for $Fe_{100-x}Ga_x$ with $x < 19$. Atomic positions were optimized according to the energy minimization procedure with a requirement that force on each atom becomes smaller than 2.0×10^{-3} a.u.

III. RESULTS AND DISCUSSIONS

Using the approach mentioned above, we calculated λ_{111} for each concentration of $Fe_{100-x}Al_x$ ($x \leqslant 25$) and $Fe_{100-x}Ga_x$

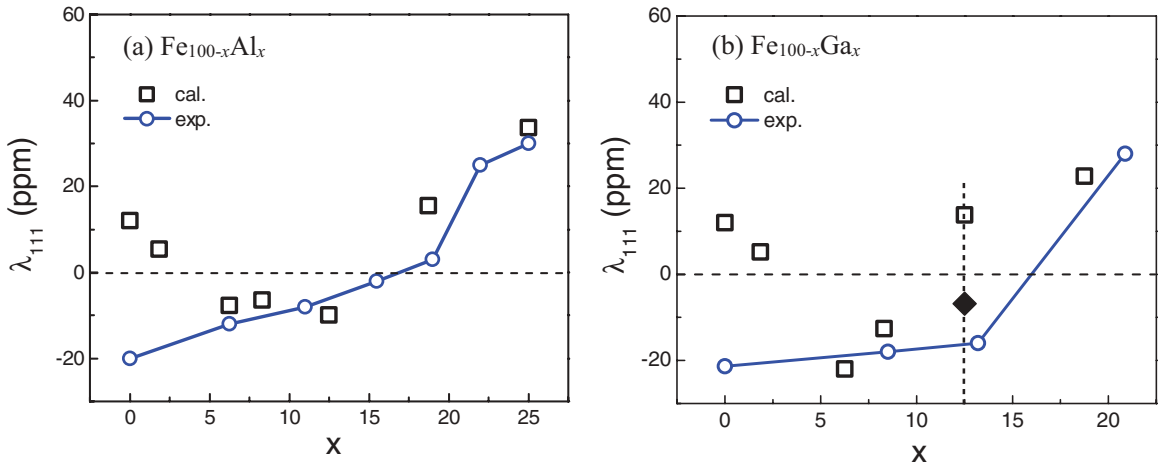

FIG. 2. (Color online) Rhombohedral magnetostrictive coefficient λ_{111} as a function of the (a) Al and (b) Ga compositions. Blue/gray circles are the experimental data from Refs. 19 and 20 for $Fe_{100-x}Al_x$ and $Fe_{100-x}Ga_x$ alloys, respectively. The filled rhombus in (b) shows a negative λ_{111} for $Fe_{87.5}Ga_{12.5}$ with the experimental lattice constant.

alloys ($x < 19$). Taking $Fe_{93.75}Al_{6.25}$ as an example, the ε dependencies of E_{MCA} and E_{tot} are shown in Fig. 1 in a range of $-2\% < \varepsilon < 2\%$. Clearly both quantities are smooth functions of ε, indicating the high quality of our theoretical data. By fitting the $E_{tot}(\varepsilon)$ and $E_{MCA}(\varepsilon)$ curves, we obtained 114 GPa for c_{44} and 2.66 MJ/m^3 (or equivalently 2.66 MPa) for b_2, respectively. According to Eq. (3), the calculated λ_{111} of $Fe_{93.75}Al_{6.25}$ is -7.8 ppm, in good agreement with the experimental result of -11 ppm.[19]

The x-dependent rhombohedral magnetostrictive coefficients of $Fe_{100-x}Ga_x$ and $Fe_{100-x}Al_x$ are given in Fig. 2, together with the corresponding experimental data.[19,20] Clearly DFT calculations achieved quantitative agreement with experimental results for λ_{111} in a wide range of x, except in the vicinity near $x = 0$. We save the arguments for the discrepancy between theory and experiment for λ_{111} near $x = 0$ at the end of this paper. As shown in Fig. 2(a), λ_{111} of $Fe_{100-x}Al_x$ remains around -9 ppm near $x = 12.5$, suddenly changes its sign from negative to positive near $x = 16$, and increases monotonically afterwards up to $x = 25$. Theoretical data points nicely trace experimental results in the range of $5 < x < 25$. Similar features were also found for $Fe_{100-x}Ga_x$ but the sign change appears to happen earlier, between $8.3 < x < 12.5$, as displayed by open squares in Fig. 2(b). This is somewhat different from experimental data that shows negative λ_{111} till $x = 13$. We found that this discrepancy results from a small overestimation of lattice size for $Fe_{87.5}Ga_{12.5}$ through GGA calculations. If the lattice size is shrunk by as little as 0.5%, from the optimized value of 2.903 Å to the experimental value of 2.889 Å,[21,22] λ_{111} of $Fe_{87.5}Ga_{12.5}$ changes to -6.8 ppm, as shown by the filled rhombus in Fig. 2(b). Further compression of lattice by another 0.5% leads to $\lambda_{111} = -12.5$ ppm, close to the experimental value of -16 ppm for $Fe_{86.8}Ga_{13.2}$. Evidently, λ_{111} is sensitive to the size of lattice and extra carefulness is necessary in this critical region.

It is instructive to separately analyze the x dependencies of b_2 and c_{44}, the numerator and denominator in Eq. (3). Again, theoretical results of both b_2 and c_{44} are comparable to the corresponding experimental data in Fig. 3.[20,23,24] One can see that c_{44} only increases slightly with the concentration of metalloid atoms for both $Fe_{100-x}Al_x$ and $Fe_{100-x}Ga_x$. The behavior of λ_{111} thus mainly relies on b_2, as shown by the similarity between the $\lambda_{111}(x)$ and $b_2(x)$ curves in Figs. 2 and 3. Comparing the calculated c_{44} and b_2 of $Fe_{87.5}Ga_{12.5}$ with optimized lattice size (open square) and experimental lattice size (filled rhombus) in Fig. 3(b), we see clearly that lattice shrinkage sensitively affects b_2 but not c_{44}. Another important aspect of λ_{111} is its small magnitude, compared to the λ_{100} at the corresponding compositions.[10] This is simply because of the large c_{44} in the entire composition range, whereas the tetragonal shear moduli $[c' = (c_{11} - c_{12})/2]$ decreases linearly with x. The magnitude of b_2 in $Fe_{100-x}Ga_x$ and $Fe_{100-x}Al_x$ is actually very close to that of the tetragonal magnetoelastic constant b_1. The origin of anisotropic mechanical responses to tetragonal and rhombohedral stresses was attributed to the formation of hingelike network of Fe bonds in the $D0_3$-like structures or, more fundamentally, to the tendency that Ga and Al atoms tend to stay apart in the Fe lattice.[25]

The satisfactory quality of theoretical data for both λ_{100} and λ_{111} with identical structural models and computational parameters indicates the reliability and predictability of the present DFT approach for studies of magnetostriction of $Fe_{100-x}Ga_x$ and sister alloys. Their monotonic enhancement of tetragonal magnetostriction and sign change of rhombohedral magnetostriction are caused by the same intrinsic electronic effects. As was discussed more extensively in Ref. 9, fundamental properties such as density of states (DOS) and wave functions indicate the development of nonbonding states around the Fermi level (E_F) as the concentration of metalloid atoms increases. Curves of total DOS in Fig. 4(a) show

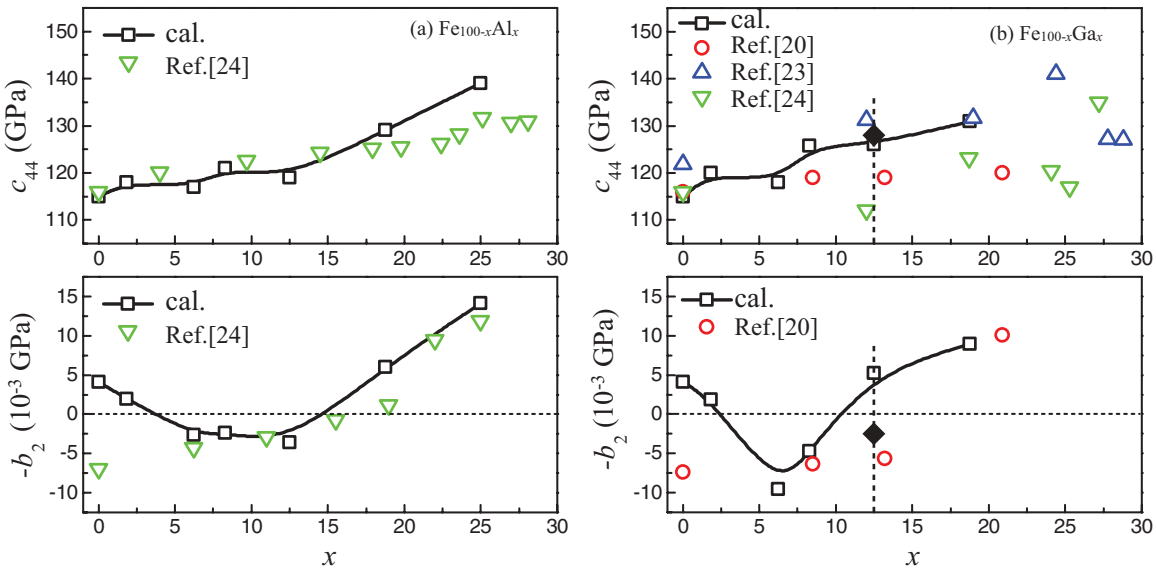

FIG. 3. (Color online) Calculated c_{44} (upper panel) and $-b_2$ (lower panel) of (a) $Fe_{100-x}Al_x$ and (b) $Fe_{100-x}Ga_x$, along with the experimental data. Open circles and down-triangles denote experimental results from Refs. 20 and 24, respectively, obtained at room temperature; open up-triangles are the results in Ref. 23 for furnace cooled samples at 4 K. Filled rhombi in (b) give results for $Fe_{87.5}Ga_{12.5}$ with the experimental lattice constant.

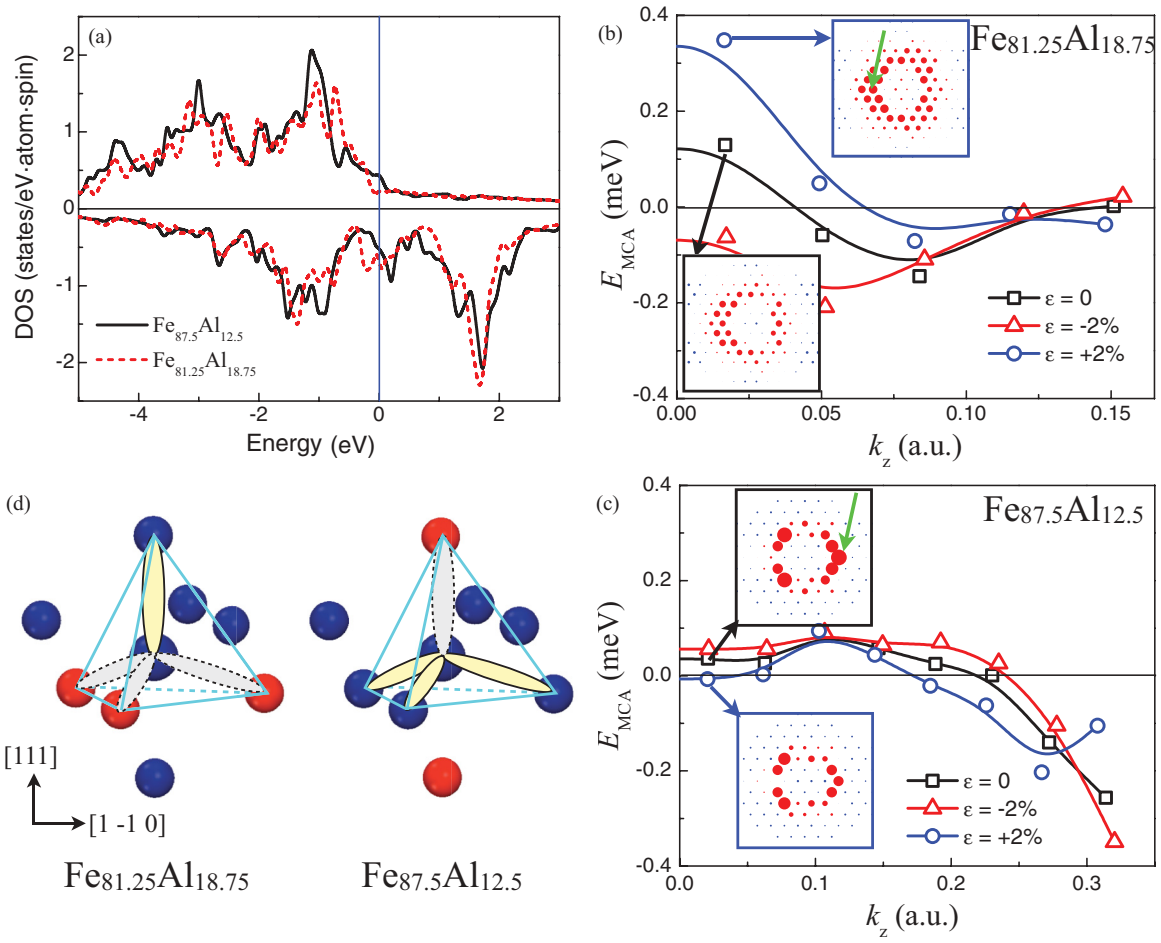

FIG. 4. (Color online) (a) Total density of states of $Fe_{87.5}Al_{12.5}$ (solid lines) and $Fe_{81.25}Al_{18.75}$ (dashed lines) alloys. Positive and negative regions are for the spin-up and spin-down parts, respectively. Zero energy indicates the position of the Fermi level. (b) The distribution of E_{MCA} along the k_z axis in the 3D BZ of $Fe_{81.25}Al_{18.75}$. Black squares, blue circles (dark gray), and red triangles (light gray) are for cases with $\varepsilon = 0\%$, $+2\%$, and -2%, respectively. The insets display the distributions of corresponding E_{MCA} in the lateral planes near $k_z = 0$. Red (light gray) and blue (dark gray) spots are for positive and negative contributions to E_{MCA} at different k points and their size scales with the magnitude of E_{MCA}. (c) The same as (b) but for $Fe_{87.5}Al_{12.5}$. The arrows in (b) and (c) highlight the hot zones of E_{MCA} in BZ that show significantly responses to strains. (d) The schematic diagram of bonds around the Fe(I) atoms in $Fe_{81.25}Al_{18.75}$ (left side) and $Fe_{87.5}Al_{12.5}$ (right side).

some distinctions between alloys with low x (less nonbonding states around E_F for $Fe_{87.5}Al_{12.5}$ with negative λ_{111}) and high x (more nonbonding states around E_F for $Fe_{81.25}Al_{18.75}$ with positive λ_{111}) in the minority spin channel. Because magnetic anisotropy and magnetostriction strongly depend on SOC interactions between states across the Fermi level,[26] the reduction in energy separation between the occupied and unoccupied states makes the SOC contributions large and easy to change, based on the second perturbation theory.

To unravel the driving factors for the sign change of λ_{111}, we split the contributions of E_{MCA} from different spin channels by turning on and off SOC in different blocks of the Hamiltonian matrix.[15] For the convenience of discussions, we use U and D to denote majority and minority spins, respectively. It was found that SOC interactions merely between states in the minority spin channel, denoted as E^{DD}, play the dominant rule for the strain-induced change of E_{MCA}. For example, values of E^{DD} for the $Fe_{81.25}Al_{18.75}$ alloy are -0.160 and 0.309 meV for $\varepsilon = 0\%$ and 2%, respectively. These are much larger than E^{UD} and E^{UU} as shown in Table I. Furthermore, by turning on and off SOC contributions from different atoms, we found that the first neighboring Fe atoms of Al or Ga [denoted as Fe(I)] provide sizable contributions to E_{MCA} and λ_{111} (see Table I). On the contrary, contributions from the second neighboring Fe atoms of Al or Ga [denoted as Fe(II)] are noticeably smaller.

We further resolve the strain induced E_{MCA} in the hexagonal Brillouin zone that has its "z axis" along the (111) direction of the conventional cubic one. Note this selection is only for the technical convenience in our calculations, and the identification of "hot" regions in BZ is not affected. The $E_{MCA} \sim k_z$ curve for unstrained $Fe_{81.25}Al_{18.75}$ in Fig. 4(b) ($\varepsilon = 0$, black squares) shows positive contributions in the region $0 < k_z \leqslant 0.04$ (a.u.) and negative contributions in the region $0.04 < k_z < 0.15$ a.u. A positive strain ($\varepsilon = +2\%$, blue circles) shifts the entire $E_{MCA} \sim k_z$ curve upward for $k_z < 0.12$ a.u., which produces more positive E_{MCA} and subsequently a positive λ_{111}. We then analyze the distribution of E_{MCA} in the lateral k plane near $k_z = 0$ for $\varepsilon = 0$ and $+2\%$, as shown in the insets in Fig. 4(b). Here red and blue dots

TABLE I. Contributions to E_{MCA} (meV) from spin-orbit couplings between different spin blocks and two types of Fe atoms in $Fe_{81.25}Al_{18.75}$ under 0% and +2% strains (ε) along the (111) direction. Here U and D denote majority spin and minority spin states involved in the SOC interactions, respectively.

ε	DD	UD	UU	Fe(I)	Fe(II)	E_{MCA}(tot)
0%	−0.160	−0.049	0.033	0.151	−0.008	−0.180
2%	0.309	0.183	0.101	0.303	0.109	0.552

represent positive and negative E_{MCA}; and their size scales with the magnitude of E_{MCA} at each k point. The most pronounced features in both insets are the rings of red dots around the center of BZ, as highlighted by the arrow in Fig. 4(b). It is obvious that both the number and size of red dots increase when a +2% strain is applied along the (111) axis. This leads to more positive E_{MCA} near $k_z = 0$, as displayed by the $E_{MCA} \sim k_z$ curve. On the contrary, the magnetostrictive response of $Fe_{87.5}Al_{12.5}$ is less pronounced near $k_z = 0$ due to less availability of dangling bonds, as displayed in Fig. 4(c). The shrinkage of the ring of red dots in the insets in Fig. 4(c) indicates that a +2% strain reduces positive contributions to E_{MCA}. In fact, this occurs almost in the entire range of k_z, except in regions around $k_z = 0.1$ a.u. and $k_z > 0.3$ a.u. Accordingly, this explains why $Fe_{87.5}Al_{12.5}$ has a negative λ_{111}.

Now we may focus on band features around the hot zones in BZ to identify the key electronic states that are responsible for the sign change of λ_{111}. Analyses in both real and reciprocal spaces reveal the importance of dangling bonds around Fe(I), as depicted by the dashed ellipses in the schematic bond diagrams in Fig. 4(d). In $Fe_{81.25}Al_{18.75}$, Fe(I) atoms take the centers of tetrahedra formed by three Al atoms and one Fe atom. As a result, three bonds around this Fe(I) atom are broken and one bond along the (111) direction is strengthened. The SOC interaction between these nonbonding states contributes to positive E_{MCA} since they have the same magnetic quantum number around the z axis. In contrast, the dangling bond around the Fe(I) atom in $Fe_{87.5}Al_{12.5}$ is along the (111) direction so the magnetic quantum number is zero around the z axis. As a result, this state does not directly contribute to E_{MCA}.

Finally, let us come back to the question: "why DFT produces a wrong sign for λ_{111} of sparse Fe alloys, or even for the pure bulk Fe?" Besides the reasons we mentioned in the Introduction, here we propose another possibility: Presence of a small percentage of interstitial impurities such as C and Si in experimental samples.[27,28] It has been seen by x-ray that bcc iron specimens with 0.03–0.06 wt. % interstitial carbon have significant local distortions.[29] The long-range lattice distortion triggered by impurity atoms is also shown in Fig. 5(a) with one carbon atom in a supercell of 128 Fe atoms. After structural optimization, we found that the presence of an interstitial carbon atom changes the c/a ratio of unit cell to 1.045 and displaces most Fe atoms, by as much as 0.33 Å along the [001] direction.

Since direct calculations for magnetostriction of large supercells are still very demanding, we examined the influence of symmetry reduction by moving the central Fe atom [Fe(C)] against the corner one either along (001) or (110) directions in a two-atom cubic unit cell. Figure 5(b) shows the calculated strain dependent E_{tot} and E_{MCA} of this "hypothetical" Fe lattice, with the Fe(C) atom 0.1 Å away from its ideal position along the (110) direction. It is interesting to see that the $E_{MCA}(\varepsilon)$ curves become nonlinear and, in particular, the slope of $E_{MCA}(\varepsilon)$ changes to negative around $\varepsilon = 0$. This indicates that sign of λ_{111} may become negative if sufficient lattice distortion is introduced. Meanwhile, our calculations indicate that the sign of λ_{100} still remains positive for this distorted Fe lattice. Experimental work to determine possible distortions in bcc Fe, as well as new values of b_2 and λ_{111} with purer Fe single crystal samples, would be valuable to solve this puzzle.

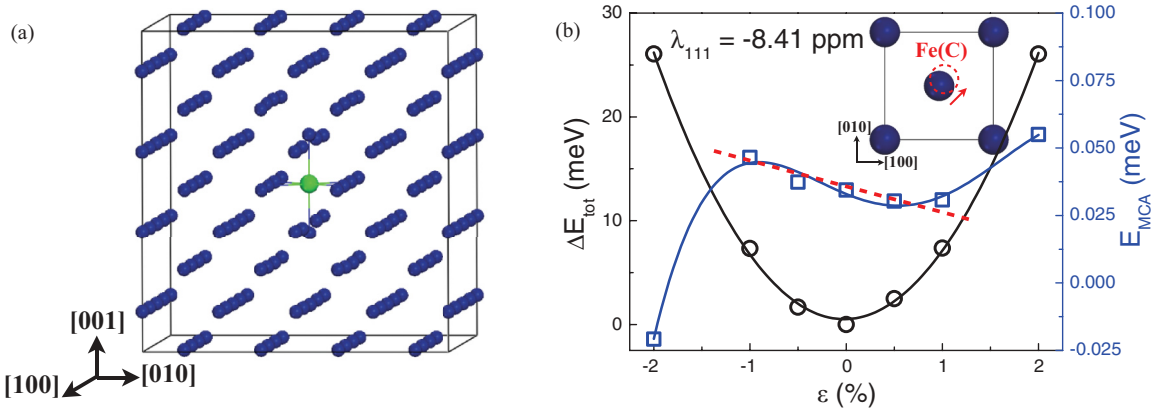

FIG. 5. (Color online) (a) The optimized geometry of the supercell with 128 Fe atoms (blue balls) and one carbon atom (green ball). (b) Calculated E_{tot} and E_{MCA} of the "distorted" Fe lattice as a function of strain along the (111) direction. The inset in (b) is a schematic diagram for the shift of the Fe(C) atom. The dashed line shows the linear fitting to the $E_{MCA} \sim \varepsilon$ curve around $\varepsilon = 0$.

IV. CONCLUSIONS

In summary, we performed systematic DFT calculations for the rhombohedral magnetostrictive coefficient λ_{111} of $Fe_{100-x}Ga_x$ and $Fe_{100-x}Al_x$ alloys with $x < 25$. The calculated λ_{111} are in consistent with experiments in a wide range of x, except in the vicinity near $x = 0$. The diagonal shear modulus c_{44} remains large in the entire range of x, so the magnitude of λ_{111} is small and the behavior of $\lambda_{111}(x)$ curves mainly relies on b_2 for both $Fe_{100-x}Al_x$ and $Fe_{100-x}Ga_x$ alloys. Analyses on the fundamental electronic properties show that the availability and local symmetry of nonbonding states near the Fermi level play an important role in determining the sign of λ_{111}. Moreover, the sign difference between experiment and theory for λ_{111} of the bulk Fe may not result from deficiencies of approximate exchange-correlation functionals, but from a small atomic displacement due to the presence of impurities. Good agreements for both tetragonal and rhombohedral magnetostrictive behaviors in a broad composition range indicate the validity and predictability of the present theory and structural models for studies of magnetostriction of transition metal alloys.

ACKNOWLEDGMENTS

The authors thank Dr. A.E. Clark, Dr. K.B. Hathaway, and Dr. M. Wun-Fogle for insightful discussions. Work was supported by the ONR (Grant No: N00014-11-1-0144). Calculations were performed on the DoD supercomputers.

[1] A. E. Clark and K. B. Hathaway, *Handbook of Giant Magnetostrictive Materials*, edited by G. Engdahl (Academic, San Diego, 2000), Chap. 1, pp. 1–48.
[2] A. E. Clark, J. B. Restorff, M. Wun-Fogle, T. A. Lograsso, and D. L. Schlagel, IEEE Trans. Magn. **36**, 3238 (2000).
[3] A. E. Clark, M. Wun-Fogle, J. B. Restorff, T. A. Lograsso, and J. R. Cullen, IEEE Trans. Magn. **37**, 2678 (2001).
[4] J. R. Cullen, A. E. Clark, M. Wun-Fogle, J. B. Restorff, and T. A. Lograsso, J. Magn. Magn. Mater. **226-230**, 948 (2001).
[5] R. Q. Wu, J. Appl. Phys. **91**, 7358 (2002).
[6] E. M. Summers, T. A. Lograsso, and M. Wun-Fogle, J. Mater. Sci. **42**, 9582 (2007).
[7] Q. Xing, Y. Du, R. J. McQueeney, and T. A. Lograsso, Acta. Mater. **56**, 4536 (2008).
[8] J. Atulasimha and A. B. Flatau, Smart Mater. Struct. **20**, 043001 (2011).
[9] G. Petculescu, R. Q. Wu, and R. McQueeney, *Handbook of Magnetic Materials*, edited by K. H. J. Buschow (Elsevier, New York, 2012), Vol. 20, Chap. 3, pp. 123-223.
[10] Y. N. Zhang, J. X. Cao, and R. Q. Wu, Appl. Phys. Lett. **96**, 062508 (2010).
[11] Y. N. Zhang and R. Q. Wu, IEEE Trans. Magn. **47**, 4044 (2011).
[12] Q. Xing and T. A. Lograsso, Appl. Phys. Lett. **93**, 182501 (2008).
[13] Y. Du, M. Huang, T. A. Lograsso, and R. J. McQueeney, Phys. Rev. B **85**, 214437 (2012).
[14] A. G. Khachaturyan and D. Viehland, Metall. Mater. Trans. A **38**, 2317 (2007).
[15] R. Q. Wu and A. J. Freeman, J. Magn. Magn. Mater. **200**, 498 (1999).
[16] M. Fähnle, M. Komelj, R. Q. Wu, and G. Y. Guo, Phys. Rev. B **65**, 144436 (2002).
[17] E. Wimmer, H. Krakauer, M. Weinert, and A. J. Freeman, Phys. Rev. B **24**, 864 (1981); M. Weinert, E. Wimmer, and A. J. Freeman, *ibid.* **26**, 4571 (1982).
[18] J. P. Perdew, K. Burke, and M. Ernzerhof, Phys. Rev. Lett. **77**, 3865 (1996).
[19] R. C. Hall, J. Appl. Phys. **30**, 816 (1959).
[20] A. E. Clark, K. B. Hathaway, M. Wun-Fogle, J. B. Restorff, T. A. Lograsso, V. M. Keppens, G. Petculescu, and R. A. Taylor, J. Appl. Phys. **93**, 8621 (2003).
[21] N. Srisukhumbowornchai and S. Guruswamy, J. Appl. Phys. **90**, 5680 (2001).
[22] H. Okamoto, Bull. Alloy Phase Diagrams **11**, 576 (1990).
[23] G. Petculescu, K. B. Hathaway, T. A. Lograsso, M. Wun-Fogle, and A. E. Clark, J. Appl. Phys. **97**, 10M315 (2005).
[24] H. M. Schurter, M.S. thesis, University of Maryland, 2009.
[25] Y. N. Zhang, R. Q. Wu, H. M. Schurter, and A. B. Flatau, J. Appl. Phys. **108**, 023513 (2010).
[26] D. S. Wang, R. Q. Wu, and A. J. Freeman, Phys. Rev. B **47**, 14932 (1993).
[27] M. Onink, C. M. Brakman, F. D. Tichelaar, E. J. Mittemeijer, S. van der Zwaag, J. H. Root, and N. B. Konyer, Scr. Metall. Mater. **29**, 1011 (1993).
[28] C. Wert, Acta Matellurgica **2**, 361 (1954).
[29] G. K. Williamson and R. E. Smallman, Acta Crystallogr. **6**, 361 (1953).